Laboratory Calibration of the Optical Transient Detector and the Lightning Imaging Sensor

WILLIAM J. KOSHAK,* MIKE F. STEWART,+ HUGH J. CHRISTIAN,* JAMES W. BERGSTROM,#
JOHN M. HALL,@ AND RICHARD J. SOLAKIEWICZ&

* *Global Hydrology and Climate Center, NASA MSFC, Huntsville, Alabama*
+ *Earth System Science Center, University of Alabama in Huntsville, Huntsville, Alabama*
# *Ball Aerospace and Technologies Corporation, Boulder, Colorado*
@ *Computer Sciences Corporation, Huntsville, Alabama*
& *Department of Mathematics and Computer Science, Chicago State University, Chicago, Illinois*

(Manuscript received 21 April 1999, in final form 8 September 1999)

ABSTRACT

The authors present in detail the laboratory apparatus and techniques that were used to complete a full radiometric calibration of two space-based lightning detectors: the optical transient detector (OTD) and the lightning imaging sensor (LIS) that were developed at the National Aeronautics and Space Administration Marshall Space Flight Center. These instruments are nadir-staring imagers that are optimized to detect and locate lightning from low-Earth orbit during day and night conditions. The radiometric calibration consisted of characterizing the pixel response to steady and transient optical sources, sensor field of view, and sensor spectral response. The transient optical signals produced in the calibration laboratory were used to derive estimates of sensor lightning detection efficiency.

1. Introduction

Some general scientific objectives of space-based lightning observations have been provided in Davis et al. (1983) and basic sensor design features of a geosynchronous lightning mapper are provided in Christian et al. (1989). In recent years, the National Aeronautics and Space Administration (NASA) Marshall Space Flight Center (MSFC) has developed two low-Earth orbit lightning detectors: the optical transient detector (OTD) and the lightning imaging sensor (LIS). The OTD is a small solid state, wide field-of-view (FOV) spaceborne sensor that detects, determines the optical intensity of, and geolocates lightning from an orbital altitude of 750 km. It was launched on a Pegasus rocket in April 1995, and currently orbits the earth aboard *OV-1* (formerly named *MicroLab-1*). OTD represents an early flight-qualified version of LIS. The LIS was launched into low-Earth orbit (350 km) in November 1997 as part of the Tropical Rainfall Measuring Mission and is described in Christian et al. (1992).

Although the diffuse upward reflection of solar radiation from the top of a thundercloud is many times brighter than diffuse cloud-top lightning emissions (Christian and Goodman 1987; Goodman et al. 1988), OTD and LIS employ special filtering techniques that allow for the detection of lightning during the day as well as at night (Christian et al. 1989). To enhance performance, the sensors also capture background images of both ground and cloud features in the near infrared. The sensor bandpass is ~1 nm and is centered near 777.4 nm, that is, near a prominent oxygen emission line triplet (777.20, 777.42, and 777.54 nm) in the lightning spectrum. The geolocated lightning event data and background images together form a lightning scene time series along the orbital track of the sensor.

Overall, OTD and LIS are composed of five major subsystems including an imaging system, a focal plane assembly [includes a charge-coupled device (CCD) array], a real-time event processor with background subtractor, a power supply, and interface electronics. The imaging system is a wide FOV lens consisting of a beam expander, a narrowband interference filter, and reimaging optics.

The frame integration time of the CCD array is ~2 ms, more than twice as long as the duration of a typical cloud-top lightning optical pulse. Once the optical pulse radiance data have been digitized and time stamped, they are combined with pixel location coordinates and are stored into an internal buffer. The data packets are shipped to spacecraft memory where it awaits subse-

Corresponding author address: Dr. William Koshak, Global Hydrology and Climate Center, NASA MSFC/SD60, 977 Explorer Blvd., Huntsville, AL 35806.
E-mail: william.koshak@msfc.nasa.gov

quent telemetry to ground. Several adjacent pixels can be illuminated by one optical pulse, and a single lightning flash can consist of several optical pulses over several frames. The raw telemetry data are processed at the ground to derive individual lightning flashes and to filter nonlightning related phenomena (e.g., solar glint, high-energy particles, background noise, etc.).

During the developmental phase of the OTD, an intensive effort was initiated to assemble an optical calibration facility for the sensor. The facility includes four radiometric tests: 1) DC linearity response and uniformity, 2) FOV, 3) spectral, and 4) transient response. Initial considerations for these tests can be found in Bergstrom et al. (1992).

In this work, we summarize the details of the laboratory apparatus and techniques that were used to complete a full radiometric calibration of the OTD and LIS. We provide basic radiometric calibration results and discuss the laboratory methods applied to estimate lightning detection efficiency. We also include a detailed discussion of the process of lightning geolocation since this is intimately linked to FOV calibration results. It is hoped that this material will aid future users of the OTD and LIS datasets by providing a basic knowledge to adequately interpret and apply the data in scientific analyses.

2. The DC response

Figure 1 summarizes the DC response test; a layout drawing of the apparatus is provided in Fig. 1a and a block diagram of the overall system, including data acquisition hardware, is given in Fig. 1b. The primary component in this test is an Optronics Laboratories, Inc., integrating sphere calibration standard (model OL 455-8-1). The 8-in. sphere lamp source emits a DC radiance that is nearly isotropic and uniform over the 2-in.-diameter exit port (source stability at 3000-K color temperature is specified at $\pm 0.5\%$ over a 1-h duration, and $\pm 2.0\%$ over the time span of a year or 100 h of use). The radiance is continuously adjustable over a range of five orders of magnitude without changing the color temperature.

Since the output cannot fill the sensor FOV, a motorized positioning system (containing Newport/Klinger rotation stages #RTN160PP with 180-kg vertical load capacity, 0.01° accuracy, 0.001° step size, and 0.001° repeatability) is used to yaw and pitch the sensor head to effect full FOV coverage. As shown in Fig. 1a, the sensor head assembly is mounted to this system. The positioner provided accurate yawing and pitching of the sensor head so that any pixel across the CCD could be illuminated. The positioning system is used in several other radiometric tests described later.

Note from Fig. 1b that an 8-bit frame grabber board is implemented as part of the lightning calibration computer. This allowed real-time display of the CCD array output (capture rate was approximately one video image

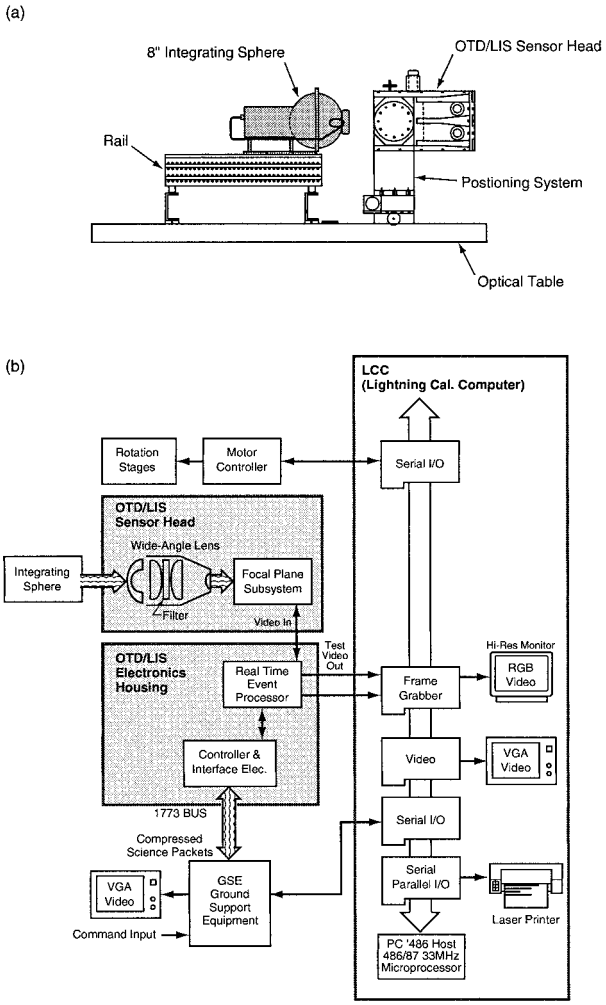

FIG. 1. The DC response test system (a) layout and (b) block diagram. This test determines pixel linearity and uniformity.

per second). The frame grabber is an integral component and diagnostic tool in all other tests described later.

The DC test determines the end-to-end radiant responsivity of each pixel to a steady optical source. Each pixel has an offset and linearity that was specifically characterized by recording the 12-bit background data as the integrating sphere output was varied over the full background range expected from diffuse cloud-top reflections of solar radiation, that is, as follows: 0.0, 66.2, 132.4, 198.6, 264.8, 331.0 W m^{-2} sr^{-1} μm^{-1}. The value 331 W m^{-2} sr^{-1} μm^{-1} is obtained by assuming a bright (albedo = 0.9) isotropic scattering cloud field that is illuminated by normal Sun incidence ($\cong$1200 W m^{-2} μm^{-1} at 777.4 nm); slight modifications for solar absorption effects were also included. The other (lower) values that are provided represent low Sun angle incidence and/or low cloud-albedo cases. Most lightning is associated with cumulonimbus clouds, and these clouds typically have albedos near 0.9 (Sellers 1965; chapter 3).

The working standard of radiance used to calibrate

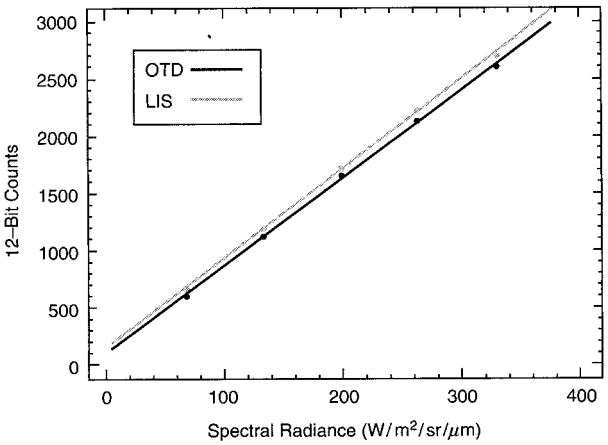

FIG. 2. Sample linearity plots for pixel (41, 92) in the OTD and LIS CCD array.

the DC response and uniformity of the instrument was the 8-in. integrating sphere. The sphere was originally calibrated by its manufacturer to a tolerance of ±3%. Since the source would by necessity receive heavy usage, in-house recalibration was performed. Because the OTD and LIS operate over a very narrow wavelength region, the luminance monitor of the sphere was modified to respond to a 13.5-nm band centered about our wavelength of interest. Thus the monitor is an accurate measure of the spectral radiance of interest. Periodic recalibration of the sphere output is necessary only to account for aging in the monitor system, that is, detector, filter, and electronics. Aging of the lamp is essentially a second-order consideration since the spectral radiance output is always set to the correct monitor value by an adjustable aperture.

A Quantum Efficient Detector (model QED-200) from Graseby Optronics, Inc., is the in-house standard used for recalibrating the sphere. The QED-200 was originally specified with a quantum efficiency of 99.9% or better. It needs yearly testing to account for aging. The detector is used with calibrated apertures and a filter to measure the average spectral radiance near 777.4 nm.

The isotropy of the sphere radiance was verified by a radiometer with the same entrance pupil diameter and location as the sensors under test. By rotating (scanning) the radiometer over the angular range of interest, the sphere radiance was found to vary by $<0.75\%$.

Figure 2 shows a typical DC responsivity plot for pixel (41, 92) in both the OTD and LIS CCD array. Note that the response is highly linear (i.e., the OTD linear regression coefficient was $r = 0.9997$). The slope and y intercept of all pixel responsivity plots were derived from this test and archived so that the actual background radiance from cloud, ground, and oceanic features is obtainable.

The question of pixel uniformity also arises. For each of the sphere output values, statistics of the mean and standard deviation of 12-bit background counts were obtained. The results for OTD are provided in Table 1. Using the ratio of the standard deviation to the mean to characterize nonuniformity, we see from Table 1 that this ratio is less than 4.5% (when all quadrants and nonzero sphere outputs are considered). Similar results were obtained for LIS. Much of this variation is due to interquadrant gain and offset differences (each quadrant has its own output amplifier resulting in slightly different gain and offset), not random fluctuations. Thus the variance could be reduced, but since it exceeds design specifications, corrections were not implemented.

3. Field of view

Figure 3 summarizes the design of the FOV test. A 9-in.-diameter, off-axis paraboloid mirror and a 1A330 ABB HAFO, Inc., infrared light-emitting diode (LED) were used. The LED had a spectral peak output at ~777 nm, a half-power bandwidth of 36 nm, and a maximum power output of 5 mW.

We used the LED to illuminate a total of 31 pixels that were evenly spaced across the CCD and we computed the associated source incidence angles (θ, φ) for each pixel using the geometrical mappings provided in Eq. (A1) of the appendix. The LED incidence angles to the lens can equivalently be viewed as lightning source angles. The geometrical mappings provided in (A1) are mathematically unique and are fundamental to the process of geolocating lightning. The extremities of the FOV were determined by simply illuminating pixels on the CCD perimeter.

The values of the source angle θ (the zenith angle to

TABLE 1. Mean 12-bit background count (and std dev) for each of the four quadrants of the OTD CCD and for each sphere stimulus. The results indicate a high degree of pixel uniformity within a single quadrant as well as between quadrants.

Sphere output (W m^{-2} sr^{-1} μm^{-1})	Quadrant I	Quadrant II	Quadrant III	Quadrant IV	All quadrants
0	131.4 (6.1)	96.5 (2.8)	112.2 (4.5)	102.1 (10.0)	110.6 (14.7)
66.2	627.7 (20.6)	593.7 (22.5)	615.2 (22.3)	615.4 (25.6)	613.0 (25.9)
132.4	1130.0 (39.7)	1102.9 (45.4)	1122.4 (43.0)	1136.9 (47.3)	1123.0 (45.8)
198.6	1632.0 (58.6)	1614.6 (69.1)	1625.4 (63.4)	1664.6 (71.6)	1634.2 (68.5)
264.8	2129.8 (77.3)	2128.3 (93.9)	2124.0 (85.5)	2202.2 (101.1)	2146.1 (95.6)
331.0	2594.6 (91.1)	2610.1 (111.0)	2590.8 (101.9)	2693.5 (119.2)	2622.3 (114.2)

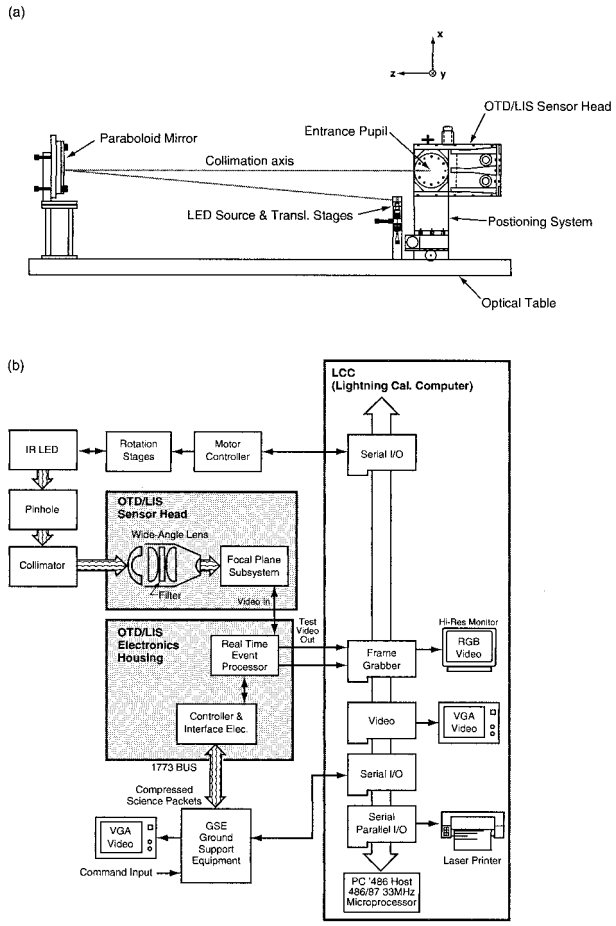

FIG. 3. The FOV test system (a) layout and (b) block diagram. This test determines the lens transfer function, the extremities of the FOV, and is fundamental to lightning geolocation.

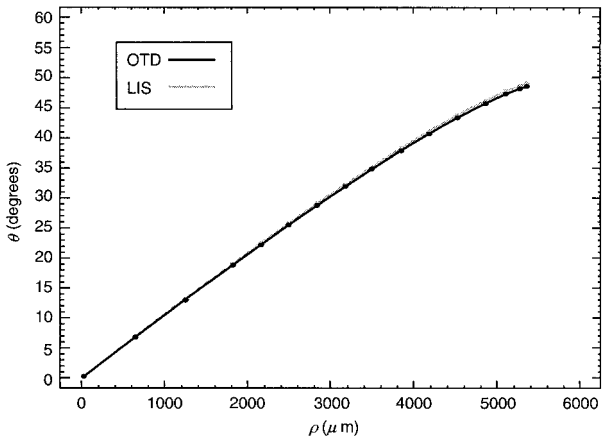

FIG. 4. The OTD and LIS lens transfer function $\theta(\rho)$. The angle θ is measured between the lens axis and the optical source. The variable ρ is the distance between the illuminated pixel and the center of the CCD array.

the CCD measured from the lens axis) were plotted against the variable ρ (the distance between the illuminated pixel and the center of the CCD). To compute ρ, a pixel dimension of 60 μm $\times$ 60 μm was used. Values of θ obtained from illuminated pixels that had similar values of ρ were averaged. The OTD and LIS lens transfer function (a spline curve fit to the θ–ρ data) is provided in Fig. 4. Since the OTD is an early version of LIS using the same lens design, the curves in Fig. 4 are very similar. Both sensors have a full FOV that is approximately square with an angular dimension of 78.5° $\times$ 78.5°. Details of how the lens transfer function is used to geolocate lightning is provided in the appendix.

4. Spectral

The spectral test is shown in Fig. 5. In Fig. 5a, a high-resolution grating monochromator (500-mm focal length, f/5 aperture, and 0.1-nm resolution) is the primary component. The attached source module contains a quartz tungsten halogen (QTH) lamp and a krypton

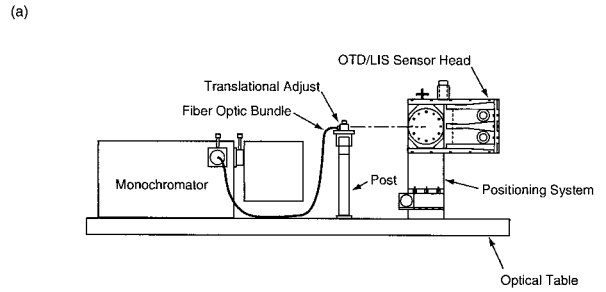

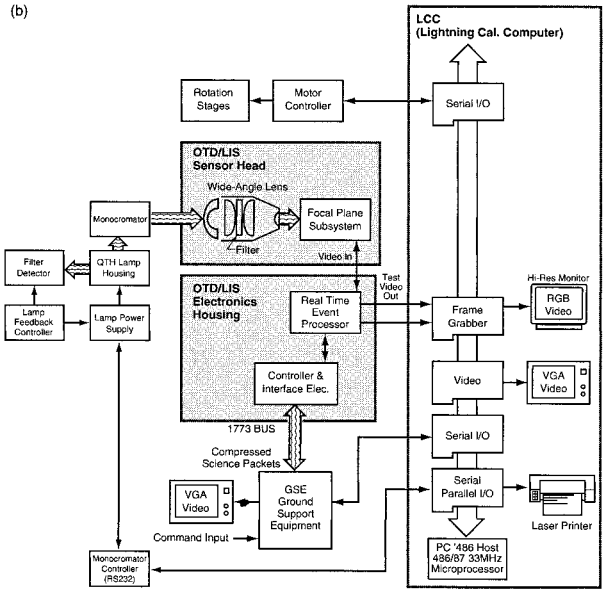

FIG. 5. The spectral test system (a) layout and (b) block diagram. This test determines the spectral response of the narrowband filter.

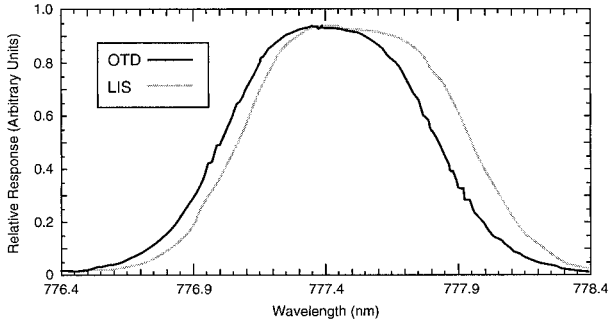

FIG. 6. Sample wavelength scans of the OTD and LIS showing the relative spectral response of the narrowband filter for pixels near the optical axis.

rare gas discharge lamp as a wavelength reference. The monochromator output is fed through a fiber-optic cable whose output is approximately collimated by a small off-axis paraboloid mirror (mirror not shown). The resultant image covered ~16 pixels. To reduce collection time while maintaining a sufficient signal-to-noise ratio, the frame grabber output from a 3×3 matrix of pixels was collected and summed for each spectral scan at various FOV locations. Figure 5b shows a block diagram including the associated data acquisition system.

Wavelength uncertainty of the spectral response measurements was monitored by repeated calibration of the monochromator to three emission lines (769.454, 774.683, and 785.482 nm) (Reader and Corliss 1980) from a low-pressure krypton lamp. A small temperature correction was also applied to compensate for temperature drifts in the monochromator. Repeatability was better than ± 0.005 nm, and absolute uncertainty was <0.015 nm.

The spectral test determines the sensor end-to-end relative spectral response. This test covered only the wavelength region near and within the passband of the narrowband interference filter. Out-of-band rejection is guaranteed by the general filter design and was verified by vendor testing.

A wavelength scan of OTD and LIS is shown in Fig. 6 for pixels located close to the center of the FOV. The OTD scan had a bandwidth at half maximum of 0.856 nm and a peak at 777.39 nm that is close to the 777.4-nm neutral oxygen emission line in the lightning spectrum (Christian et al. 1989). The LIS scan had a bandwidth of 0.909 nm and was centered closer to 777.5 nm. The 0.1-nm shift to longer wavelengths was intentional in the design of the LIS filter in order to help offset the natural shift in the curve toward shorter wavelengths for larger incidence angles. As such, the LIS filter represents a planned improvement over the earlier fabricated OTD filter. Overall, vendor fabrication of these filters was not easy. Several trials were performed to meet specifications, and minor defects in the resulting spectral curves are possible. Wavelength scans performed for pixels off-axis, that is, for large values of θ, were similar to that shown in Fig. 6, but with small shifts (<0.8 nm) to shorter wavelengths.

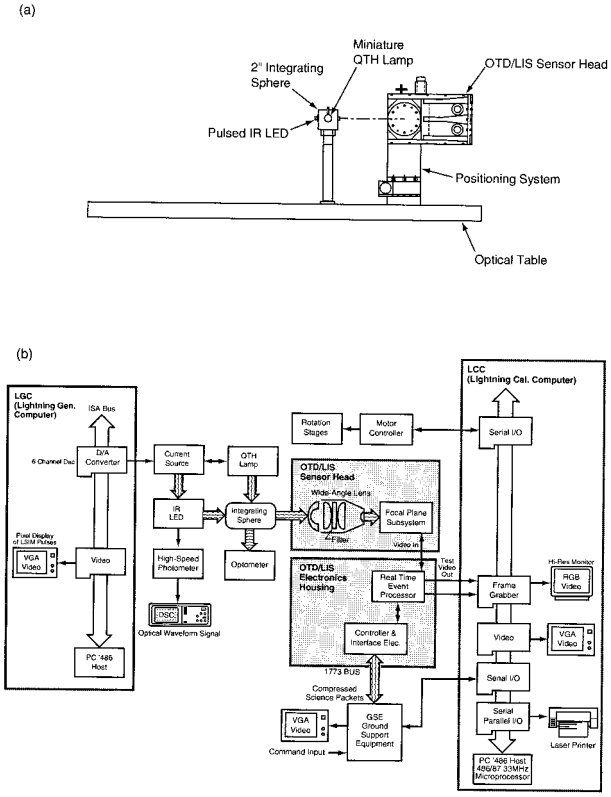

FIG. 7. The transient response test system (a) layout and (b) block diagram. This test determines the response of the sensor to optical pulses.

5. Transient response

The purpose of this test is to determine the transient response of the sensor to pulses of various integrated energies, against several different levels of steady-state background radiance, and for several different pixels across the CCD array. The OTD and LIS both have a real-time event processor that maintains a frame-by-frame estimate of the background radiance for each pixel; the frame time is ~2 ms. The background energy estimate is subtracted from a subsequent frame and if the residual exceeds a prescribed threshold, it is assumed that the pixel detected a lightning optical emission (or ''event''). The event data are further processed at NASA MSFC to remove noise. One important distinction between the AC signal channels of OTD and LIS is that the OTD employed a logarithmic amplifier, whereas LIS employed a (piecewise) linear amplifier.

Figure 7 depicts the transient response test system, with its primary component a 2-in. SPECTRALON integrating sphere containing a near-infrared (NIR) LED and a small QTH lamp. The LED was selected over a diode laser, as proposed in the earlier paper (Bergstrom

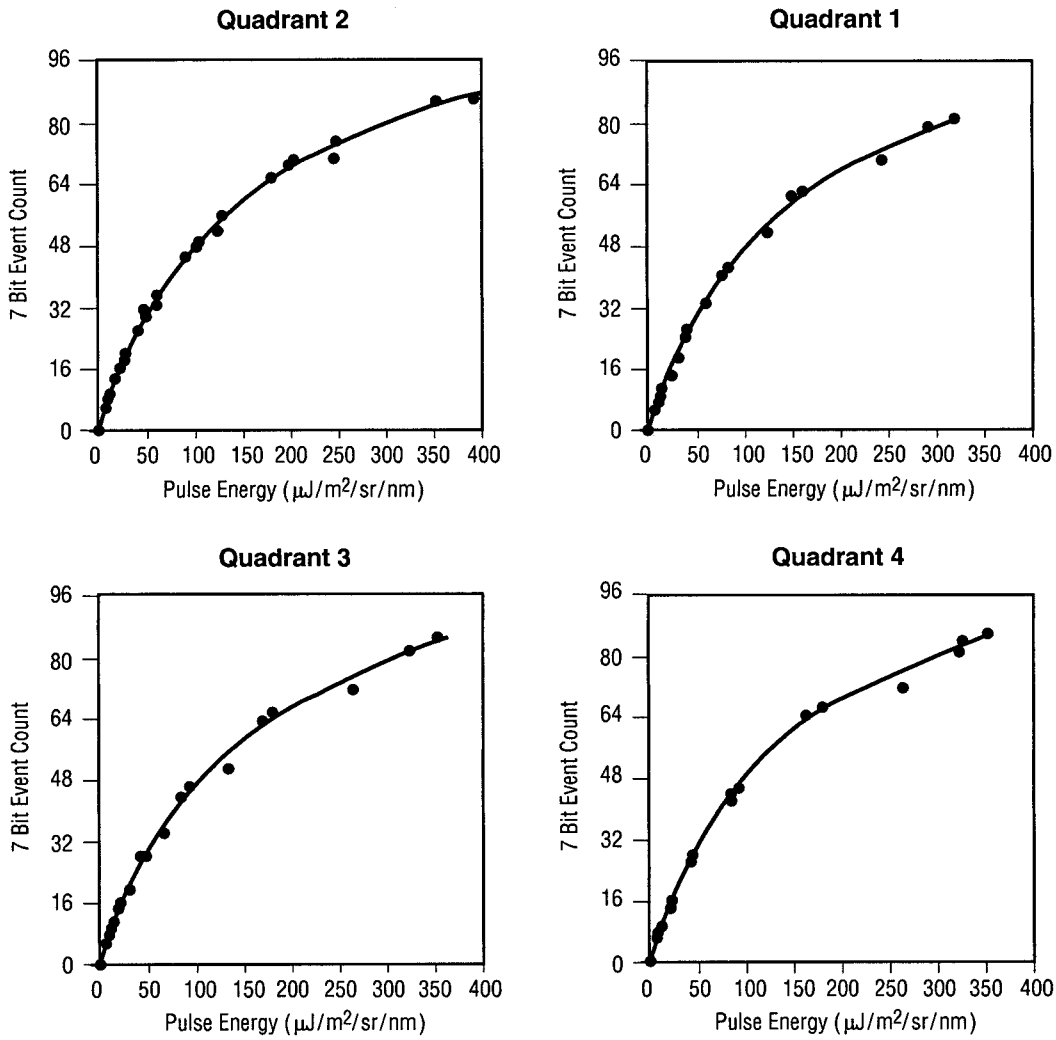

FIG. 8. The transient response curves of the OTD for each of the four quadrants in the CCD array, under nighttime conditions.

et al. 1992), to avoid uncertainties due to polarization, coherence, and temperature sensitivity. NIR LEDs were specially selected by ABB HAFO, Inc., with peak emission near 777.4-nm wavelength at room temperature. The LED is mounted behind a pinhole in the far surface of the sphere. By placing the sphere in the near field, the pulsing LED is out of focus and appears superimposed upon a nearly uniform background illumination extending over several pixels. Background radiance levels are adjusted by a variable aperture in the lamp input port, thus maintaining a constant color temperature. The time-integrated energy of the transient signal is varied over a wide dynamic range width modulation of the LED.

Absolute radiometric reference for the transient response testing is provided by ''bootstrapping'' from the previous DC response measurements of the sensor. That is, to obtain a specific background radiance from the QTH lamp in the small sphere, the lamp output is adjusted until the 12-bit count from the sensor gives the appropriate radiance (the 12-bit count and radiance values are related by the linearity results obtained from the DC response test). The LED ''equivalent DC radiance'' is found in a similar fashion. The LED is then pulsed with a constant amplitude and a range of known pulse widths to simulate the desired lightning energy range.

For OTD, a total of 14 individual regions were illuminated, and response curves (fourth-order polynomial fits to the data) were obtained for each of the four quadrants of the CCD for five different background levels (0, 63.6, 132.4, 202.6, and 273.7 W m^{-2} sr^{-1} μm^{-1}). The indicated range of values are typical of diffuse solar reflections from cloud top.

Figure 8 shows the results of this test for nighttime background conditions (lamp aperture fully closed). Abscissa values in Fig. 8 can be converted to units of microjoules per meter squared per steradian by multiplying by the mean filter bandwidth, $\Delta\lambda = 0.845$ nm.

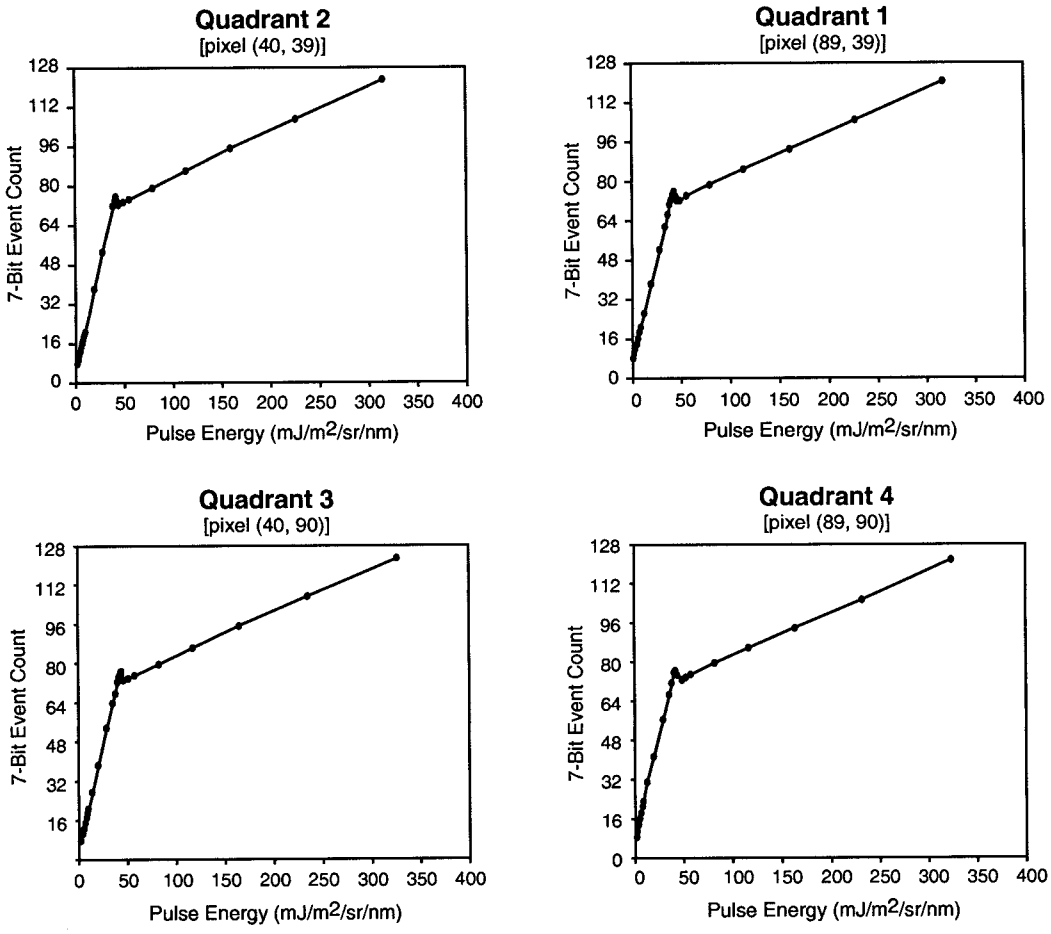

FIG. 9. Sample transient response curve for each quadrant of the LIS CCD array.

These data are fundamental to the discussion of lightning detection given below.

The transient channel electronics of the LIS had improved sensitivity. The piecewise linear response is shown in Fig. 9. The transition between the two linear regions occurs at rather large (less frequent) lightning energies [see the lightning optical pulse energy distribution provided in Christian and Goodman (1987)].

6. Lightning detection efficiency

The results provided in Figs. 8 and 9 can be compared with lightning statistics obtained from Christian and Goodman (1987) and Goodman et al. (1988) in order to estimate the sensor lightning detection efficiency (LDE). The statistics in these studies were derived from high-altitude aircraft observations of diffuse cloud-top lightning emissions. The aircraft were equipped with optical pulse sensors that detected the characteristic waveforms associated with cloud-top lightning illuminations. The optical pulse data characteristics have been examined and reproduced by Koshak et al. (1994) using a Boltzmann photon transport model for lightning sources embedded deep within a multiple scattering thundercloud medium.

It was found from the aircraft studies that cloud and ground lightning flashes can each generate as many as 40 or more optical pulses (optical pulses are primarily produced from return strokes and K changes). About 90% of the flashes had at least one pulse with an energy $>4.7\ \mu J\ m^{-2}\ sr^{-1}$. Consequently, this energy level has been cited as a trigger threshold for lightning imaging sensor technologies (Christian et al. 1989).

Figure 10 of Christian and Goodman (1987) provides the distribution of peak radiant energy per flash. Only the most intense pulse of each lighting flash was considered. If these data are replotted as a cumulative distribution (see Fig. 10 here) it can serve as an *estimate* of LDE if the minimum detectable optical pulse energy is known from laboratory calibration. [Note: The LDE is defined as the percentage of flashes (cloud or ground) within the sensor FOV that are detected. Although this definition ''lumps'' cloud and ground flashes together, the detection efficiency of cloud flashes might possibly differ from that of ground flashes.]

Using the laboratory results in Fig. 8, the mean min-

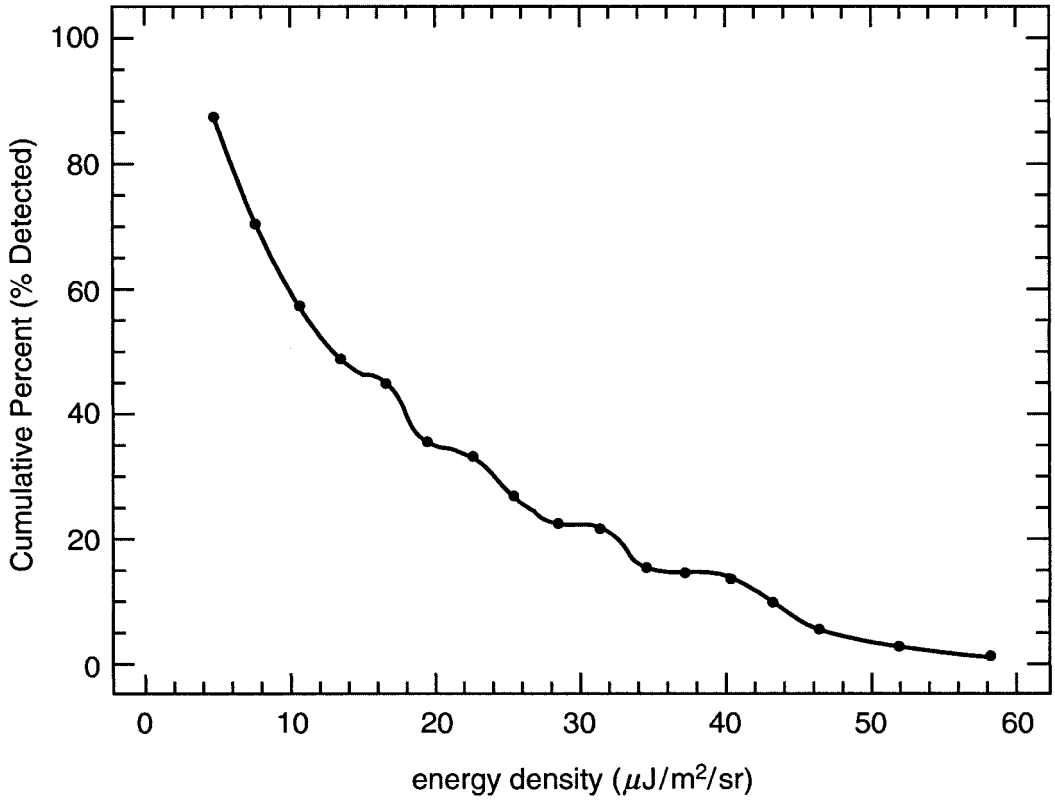

FIG. 10. A cumulative distribution of naturally occurring lightning optical energies. This plot was derived from U2 aircraft measurements provided in Fig. 10 of Christian and Goodman (1987). The plot can be used to estimate the LDE when the minimum detectable energy of the sensor is determined from laboratory calibration. Note that as the (minimum detectable) energy density decreases, the percent detected increases.

imum LED pulse energy (units: μJ m^{-2} sr^{-1}) detected by OTD from the transient test was 6.19 (quadrant I), 7.44 (quadrant II), 7.02 (quadrant III), and 6.29 (quadrant IV). From Fig. 10, this corresponds to detection efficiencies of 79%, 72%, 74%, and 77%, respectively. By a similar analysis using the data in Fig. 9, we obtain a detection efficiency of ~98% for each of the four quadrants of the LIS CCD array.

Of course, there are many assumptions leading to these estimates of LDE. For instance, Fig. 10 of Christian and Goodman (1987) was based only on 73 flashes that were observed over specific geographical areas, time of day, and season. In addition, some of the optical pulses had complicated waveforms that were not included in the statistical analysis.

Finally, the altitude of the aircraft and the 60° optical pulse sensor FOV resulted in a cloud-top areal coverage of about 4.6 km × 4.6 km. This is substantially less than the OTD resolution (~8 km at nadir, ~20 km near the edge of the FOV). Because the aircraft optical pulse sensors do not view as much of the optical emission from cloud-top as does OTD and would therefore likely miss the region of peak emission, it is likely that the aircraft statistics underestimate the peak radiant energy from a lightning flash. This would imply that the estimates of LDE for OTD provided above are too low. Of course, all laboratory estimates of LDE must be amended to reflect actual in-flight trigger threshold settings. Further, threshold settings in space could be substantially higher than the minimum setting achievable in a laboratory environment.

7. False alarm rate

In addition to normal detection, OTD and LIS will trigger or ''false alarm'' on events produced from noise in the system. For OTD, the electronic noise exceeded the photon shot noise. Because of this, a single transient channel trigger threshold was implemented independent of the particular (12 bit) background count level acquired by the pixel.

To characterize false alarm rate (FAR), the number of photoelectrons accumulated by a pixel in one (2 ms) frame time, $N = N_b + N_l + N_r$, is considered. Here, N_b is the number of photoelectrons due to the background, N_l is the number due to lightning, and N_r is the number due to electronic noise. A pixel will trigger whenever $(N - \mu) > T$, where T is the number of photoelectrons required for triggering the system and μ is the mean number of photoelectrons. In practice, the

OTD real-time event processor estimates μ by computing a sample average of N over several frames. If the system noise is Gaussian distributed with a standard deviation, $\sigma = \mu^{1/2}$, the probability of a pixel triggering is, after neglecting integrands of order $\mu/(N - \mu)^2$,

$$P(N - \mu > T) = \frac{1}{T}\left(\frac{\mu}{2\pi}\right)^{1/2} \exp\left(\frac{-T^2}{2\mu}\right). \quad (1)$$

If there is no lightning event in a frame ($N_l = 0$), but $(N - \mu) > T$ holds because of system noise, the OTD will give a false alarm. The FAR from the entire CCD array is then

$$\text{FAR} = P(N - \mu > T)[(128)^2 \text{ pixels per frame}] \times [500 \text{ frames per second}]. \quad (2)$$

In the calibration of OTD, if the 7-bit threshold was set below seven counts, the FAR was deemed unacceptable. When the threshold is increased slightly to decrease the FAR to an acceptable level, there is a slight reduction in the LDE values to 74%, 67%, 71%, 75%, for quadrants I, II, III, and IV, respectively. The tradeoff between false alarms and detectability is fundamental to many optical detection systems. Generally, we have set the sensor threshold high enough to keep the FAR well below ~10%.

8. Summary of calibration results

In this paper, we have presented an overview of the most important calibration efforts undertaken to quantify the OTD and LIS datasets. In summary, we have found that the DC response of each pixel had linear correlation coefficients that were better than 0.98, and pixel nonuniformity varied by <4.5%. The FOV was approximately square with angular dimensions 78.5° × 78.5° and the lens transfer function was highly linear over much of the FOV. Fourth-order polynomial fits were sufficient to characterize the log-amplifier transient channel of OTD; changes in the response curves for different background levels are most notable for 7-bit event counts >40 (i.e., for large, infrequent lightning pulses in excess of about 63 μJ m^{-2} sr^{-1}). The transient channel of LIS had much improved sensitivity over OTD and a piecewise linear response function. The spectral bandwidth for OTD and LIS was <1 nm and the center wavelength was close to natural lightning emission lines.

Prelaunch estimates of the OTD detection efficiency for nighttime conditions were on the order of 70%, depending on the CCD quadrant under scrutiny. It was expected that on-orbit conditions would require raising the sensor threshold, thus lowering the detection efficiency (and FAR). The rate of false triggering is primarily governed by electronic noise rather than shot noise; one specific threshold value is used for the entire CCD array independent of the background level and associated shot noise effect. The LIS detection efficiency is estimated to be ~25% better than that of OTD. Of course, all estimates of detection efficiency depend on the specific in-flight threshold settings, and these settings are routinely adjusted over the sensor lifetime to optimize data results.

In-flight monitoring of the OTD and LIS calibration is performed throughout the lifetime of the instruments. We shall continue to acquire correlated ground truth measurements (e.g., lightning detection and ranging, flash counters, field mills, magnetic direction finders, interferometers, radar, and optical pulse sensors) to compare with OTD and LIS results, and we shall use the ground truth information to assess the true detection efficiency and false alarm rate.

Acknowledgments. This work was funded under NASA Contract NAS8-97250. The authors thank Preston Hassler and Ron McIntosh of NASA MSFC for their support of several calibration facility efforts. We also appreciate the work of Susan Burrer and Kay Glover in completing the final form of this manuscript, and the work of Janine Roskowski for her help in preparing the final figures.

APPENDIX

Lightning Geolocation

In the calibration lab, a known source was used to illuminate a specific pixel in the FOV. Lightning geolocation involves the inverse process, that is, an illuminated pixel is used to determine a latitude and longitude coordinate on the surface of the earth.

To determine the geometrical mapping between source incidence and an illuminated pixel, we consider an orthogonal right-handed coordinate system ($\hat{\mathbf{x}}$, $\hat{\mathbf{y}}$, $\hat{\mathbf{z}}$) fixed to the positioning system shown in Fig. 3a. The origin of this system is at the entrance pupil of the sensor, but we have translated it vertically in Fig. 3a for clarity. Rigidly attached to this coordinate system is the "CCD system" ($\hat{\mathbf{f}}$, $\hat{\mathbf{g}}$, $\hat{\mathbf{h}}$) where ($\hat{\mathbf{f}}$, $\hat{\mathbf{g}}$) are orthogonal axes in the plane of the CCD array. The origin of the CCD system is located at the geometrical center of the CCD array. The pixel addresses of the four corners of the 128 × 128 array are defined as follows: (1, 1) = upper-left corner; (128, 1) = upper-right corner; (1, 128) = lower-left corner; and (128, 128) = lower-right corner. The unit vectors $\hat{\mathbf{f}}$ and $\hat{\mathbf{g}}$ are the respective horizontal and vertical Cartesian coordinate axes of this array. The positive horizontal direction, $\hat{\mathbf{f}}$, along the array is defined to be from pixel (1, 1) to pixel (128, 1), and the positive vertical direction, $\hat{\mathbf{g}}$, is from (1, 128) to (1, 1). Finally, $\hat{\mathbf{h}} = \hat{\mathbf{f}} \times \hat{\mathbf{g}}$ is along the sensor lens axis (assumed orthogonal to the CCD).

In mounting the sensor to the positioning system, the lens axis was largely parallel to the z axis, but the ($\hat{\mathbf{f}}$, $\hat{\mathbf{g}}$) axes were rotated with respect to the ($\hat{\mathbf{x}}$, $\hat{\mathbf{y}}$) axes by a

mechanical angle γ_m. In general, we consider the three Euler ''mechanical misalignment'' angles (α_m, β_m, γ_m) that fully determine the physical orientation between the positioning system and the CCD system. However, the first two of these Euler angles are approximately zero.

If the sensor head is arbitrarily yawed by an angle α about the $\hat{\mathbf{x}}$ axis and pitched by an angle β about the $\hat{\mathbf{y}}$ axis, the collimated beam will make an angle θ with the lens axis, $\hat{\mathbf{h}}$. The projection of the collimated beam into the plane of the CCD will make an azimuthal angle φ with the $\hat{\mathbf{f}}$ axis. Since the motor controller shown in Fig. 3b provides precise digital displays of the numerical values of the positioning system yaw, α, and pitch, β, it was desirable to express the source angles (θ, φ) directly in terms of (α, β). The geometrical mapping can be expressed as

$$\theta(\alpha, \beta) = \cos^{-1}(-H_1 \cos\alpha \sin\beta + H_2 \sin\alpha + H_3 \cos\alpha \cos\beta)$$

$$\varphi(\alpha, \beta) = \tan^{-1}\left(\frac{-G_1 \cos\alpha \sin\beta + G_2 \sin\alpha + G_3 \cos\alpha \cos\beta}{-F_1 \cos\alpha \sin\beta + F_2 \sin\alpha + F_3 \cos\alpha \cos\beta}\right), \quad \text{(A1)}$$

where the mechanical misalignment constants are given by

$$F_1 = \cos\gamma_m \cos\beta_m$$

$$F_2 = \sin\gamma_m \cos\alpha_m + \cos\gamma_m \sin\beta_m \sin\alpha_m$$

$$F_3 = \sin\gamma_m \sin\alpha_m - \cos\gamma_m \sin\beta_m \cos\alpha_m$$

$$H_1 = \sin\beta_m, \qquad H_2 = -\cos\beta_m \sin\alpha_m$$

$$H_3 = \cos\beta_m \cos\alpha_m. \quad \text{(A2)}$$

The constants G_1, G_2, and G_3 are identical with F_1, F_2, and F_3, respectively, but with $\cos\gamma_m$ replaced with $-\sin\gamma_m$ and $\sin\gamma_m$ replaced with $\cos\gamma_m$.

In order to geolocate lightning, (α_m, β_m, γ_m) must be determined. Since $\alpha_m \simeq 0$, $\beta_m \simeq 0$, it is still necessary to determine γ_m. Note that the collimated light beam direction, $\hat{\mathbf{q}}$, in the CCD reference frame is

$$\hat{\mathbf{q}}(\theta, \varphi) = \tilde{\mathbf{K}}(\alpha_m, \beta_m, \gamma_m)\hat{\mathbf{m}}(\alpha, \beta), \quad \text{(A3)}$$

where $\tilde{\mathbf{K}}$ is the Euler angle matrix whose first, second, and third row vectors are (F_1, F_2, F_3), (G_1, G_2, G_3), and (H_1, H_2, H_3), respectively, and the column vectors are $\hat{\mathbf{q}} = \text{col}(\sin\theta\cos\varphi, \sin\theta\sin\varphi, \cos\theta)$ and $\hat{\mathbf{m}} = \text{col}(-\cos\alpha \sin\beta, \sin\alpha, \cos\alpha \cos\beta)$. We refer to the unit vector $\hat{\mathbf{m}}$ as the ''mechanical vector'' since it is proportional solely to the mechanical yaw and pitch values of the positioning system. Performing the matrix multiplication in (A3), the first two components of the resulting vector equation lead to the result:

$$\theta' = \theta \qquad \varphi' = \varphi + \gamma_m, \quad \text{(A4)}$$

where the primed variables indicate the orientation of the collimated beam relative to the CCD coordinate frame *had the mechanical angle, γ_m, been zero.* Since the effect of the sensor lens is to rotate the source azimuth by 180°, the second equation in (A4) can be written

$$\gamma_m = \varphi' - (\phi + \pi), \quad \text{(A5)}$$

where ϕ is the known azimuth of the illuminated pixel in the CCD array and φ' is solely a function of the yaw and pitch angles [i.e., it is given by the second equation in (A1) with $\gamma_m \equiv 0$, and $\alpha_m \simeq 0$, $\beta_m \simeq 0$]. For example, after illuminating 31 pixels that were evenly spaced across the OTD CCD, application of (A5) provided a mean value of γ_m equal to 327.5° with a standard deviation of 0.158°.

To geolocate a lightning event, we consider a pixel in the CCD with coordinates (f, g) that has been illuminated by an optical source (e.g., lightning) located on the surface of the earth with respective latitude and longitude (ψ, λ). Geolocation is the process of mapping pixel location (f, g) to (ψ, λ).

In order to accomplish this mapping, it is useful to determine the unit vector, $\hat{\mathbf{q}}'$, that points from the spacecraft to the source. We express $\hat{\mathbf{q}}'$ in terms of a coordinate system ($\hat{\mathbf{X}}$, $\hat{\mathbf{Y}}$, $\hat{\mathbf{Z}}$) whose origin is fixed to the center of the earth. The relationship between $\hat{\mathbf{q}}'$ and the light beam direction, $\hat{\mathbf{q}}$, given in (A3) for OTD is

$$\hat{\mathbf{q}}' = \mathbf{ELASDTK}\hat{\mathbf{q}}(\theta, \varphi), \quad \text{(A6)}$$

where the transformation matrices are **K**: from CCD frame to positioning system frame, **T**: from positioning system frame to a laboratory theodolite frame, **D**: from theodolite frame to the detector alignment cube frame (defined by three of the cube faces), **S**: from detector cube frame to the spacecraft cube frame, **A**: from spacecraft cube frame to the attitude reference frame, **L**: from attitude reference frame to the local level frame (defined by the spacecraft position and velocity vector), and **E**: from the local level frame to a coordinate frame attached to the rotating earth. The last two transformations vary with time since the satellite attitude and ephemeris vary.

Accounting for the lens inversion of π radians we obtain the desired mapping

$$\hat{\mathbf{q}}'(f, g) = \mathbf{ELASDTK}\boldsymbol{\Lambda}\hat{\mathbf{p}}[\theta(\rho), \phi], \quad \text{(A7)}$$

where the azimuth of $\hat{\mathbf{p}}$ [given by the pixel azimuth ϕ

$= \tan^{-1}(g/f)$ appropriately corrected for quadrant] is rotated by π radians from $\hat{\mathbf{q}}$. The lens transfer function $\theta(\rho)$, $\rho = [f^2 + g^2]^{1/2}$, is given in Fig. 4 of section 3 and the lens inversion matrix is

$$\mathbf{\Lambda} = \begin{bmatrix} -1 & 0 & 0 \\ 0 & -1 & 0 \\ 0 & 0 & 1 \end{bmatrix}. \quad \text{(A8)}$$

The location of the source expressed in the earth frame, $\mathbf{r} = (X\hat{\mathbf{X}} + Y\hat{\mathbf{Y}} + Z\hat{\mathbf{Z}})$, can be written as the sum of the spacecraft location vector, $\mathbf{r}_s = X_s\hat{\mathbf{X}} + Y_s\hat{\mathbf{Y}} + Z_s\hat{\mathbf{Z}}$, and the vector $\zeta\hat{\mathbf{q}}'$, where ζ is a scalar multiple. That is, $\mathbf{r} = \mathbf{r}_s + \zeta\hat{\mathbf{q}}'$. The components of $\mathbf{r}$ in terms of ζ can be substituted into the ellipsoidal constraint $X^2/a^2 + Y^2/b^2 + Z^2/c^2 = 1$, which is used to model the surface of the earth. The resulting quadratic equation can be solved for ζ. Now the physical source location, $\mathbf{r}$, is known and can be appropriately converted to obtain source latitude and longitude. This summarizes the critical variables associated with the OTD geolocation process.

REFERENCES

Bergstrom, J. W., J. W. Jackson, D. E. Simmons, and H. J. Christian, 1992: Functional test and calibration plan for the lightning imaging sensor. *Proc. SPIE,* **1745,** 217–226.

Christian, H. J., and S. J. Goodman, 1987: Optical observations of lightning from a high-altitude airplane. *J. Atmos. Oceanic Technol.,* **4,** 701–711.

——, R. J. Blakeslee, and S. J. Goodman, 1989: The detection of lightning from geo-stationary orbit. *J. Geophys. Res.,* **94,** 13 329–13 337.

——, ——, and ——, 1992: Lightning imaging sensor (LIS) for earth observing system. NASA TM 4350, 1–36. [Available from Redstone Scientific Information Center, Attn: AMSAN-RD-AS-I-RSIC, Bldg. 4484, Redstone Arsenal, AL 35898-5000.]

Davis, M. H., M. Brook, H. J. Christian, B. G. Heikes, R. E. Orville, C. G. Park, R. G. Roble, and B. Vonnegut, 1983: Some scientific objectives of a satellite-borne lightning mapper. *Bull. Amer. Meteor. Soc.,* **64,** 114–119.

Goodman, S. J., H. J. Christian, and W. D. Rust, 1988: A comparison of the optical pulse characteristics of intracloud and cloud-to-ground lightning as observed above clouds. *J. Appl. Meteor.,* **27,** 1369–1381.

Koshak, W. J., R. J. Solakiewicz, D. D. Phanord, and R. J. Blakeslee, 1994: Diffusion model for lightning radiative transfer. *J. Geophys. Res.,* **99,** 14 361–14 371.

Reader, J., and C. H. Corliss, 1980: Wavelengths and transition probabilities for atoms and atomic ions—Part I: Wavelengths. U.S. Department of Commerce-NBS, Rep. NSRDS-NBS-68LC80-607997, 416 pp. [Available from National Technical Information Service, Springfield, VA 22161.]

Sellers, W. D., 1965: *Physical Climatology.* The University of Chicago Press, 272 pp.